

Enhancement of side-coupled surface plasmon resonance sensitivity by application of polymethylmethacrylate thin polymer films

Saima Amjad^{1,2}, Kankan Swargiary³, Manjunath Somarapalli³, Tanujjal Bora^{1,2}, Gabor L. Hornyak¹, Waleed S. Mohammed³ ✉

¹Center of Excellence in Nanotechnology, Asian Institute of Technology, 12120 Pathumthani, Thailand

²Nanotechnology, Industrial Systems Engineering, School of Engineering & Technology, Asian Institute of Technology, 12120 Pathumthani, Thailand

³Center of Research in Optoelectronics, Communication and Computational Systems (BU-CROCCS), School of Engineering, Bangkok University, 12120 Pathumthani, Thailand

✉ E-mail: wsoliman@gmail.com

Published in Micro & Nano Letters; Received on 12th November 2019; Revised on 16th January 2020; Accepted on 28th January 2020

Here the theoretical and experimental investigation for enhancing surface plasmon resonance (SPR) sensitivity in a side-coupled excitation system by the application of polymethylmethacrylate (PMMA) polymer thin films is presented. Proper selection of film materials, gold layer thicknesses d_{Au} and SPR incident angle (θ_{SPR}) resulted in the increased effective refractive index of the sensing region, and hence of the device sensitivity, and the dynamic detection range. This work demonstrates, by first-order approximations, a characterisation scheme of SPR chips with unknown gold layer thickness d_{Au} and uncertainty in SPR incident angle. The scheme utilised fitting theoretical calculations to measured SPR responses while varying d_{Au} and θ_{SPR} in equations. Device sensitivity nearly doubled following application of thin PMMA thin films on gold surfaces when sensing water-chloroform mixtures as opposed to untreated surfaces that lacked a PMMA layer. The proposed work demonstrates a facilitative balance between theoretical expectations and experimental data to develop sensors for future applications.

1. Introduction: In recent decades, industrialisation and commercialisation have given rise to an enormous outbreak of hazardous air pollutants, volatile organic compounds (VOCs) and other harmful components found in water and air [1]. These pollutants collectively and increasingly form a constant threat to human health and hence to life itself [2]. The alarming state of affairs requires that better schemes with higher sensitivity, selectivity, facility and utility be developed for real-time and accurate analyses. Furthermore, recent advances in remote sensing and on-sight methodologies have opened new avenues that promote effective means of identifying these harmful emissions [3]. These include gravimetric, electrical and optical methods capable of providing routine detection limits in the 10–100 ppm range [4]. Optical sensors utilising the thin-film technology are gaining rapid interest due to precise fabrication and ability to detect small environmental variations [5]. Surface plasmon resonance (SPR) is a sensitive and configuration selective optical detection technique. The fundamental mechanism of SPR is based on refractive index changes caused by adsorbed analytes onto a gold substrate resulting in shifts in the SPR wavelength (λ_{SPR}) and signal intensity [6–8]. Compact SPR systems can be realised using integrated optics where the Plasmonic sensor becomes a part of a waveguide structure [9]. In the previous work, our group introduced a low-cost SPR system housed within a three-dimensional (3D) printed architecture. In this device, excitation was provided by an ‘off-the-shelf’ white light-emitting diode (LED) source in a side-coupled configuration (a.k.a. BU-SPR) [10]. This configuration, which was originally developed by the authors, is low cost and provides average sensitivity of 10^{-4} RIU. The LED source was fixed at a specific angle (θ_{SPR}) with a relatively high angle uncertainty of ca. $\pm 5^\circ$. SPR chips were prepared by using a custom-made in-house sputtering system. The BU-SPR configuration is shown in Fig. 1. SPR device sensitivity can be improved by changing the substrate material [11] optical properties or surface functionalisation such as adding a mono-graphene layer [12]. Here we describe a method that improved the performance of the BU-SPR sensor in terms of

λ_{SPR} resolution, dynamic range and signal intensity by fine-tuning operation parameters and by application of thin polymethylmethacrylate (PMMA) films that increased the effective refractive index of the system. A signal processing approach is adopted in this work for the experimental correlation with theoretical calculations.

2. Methodology overview: The methodology was divided into three parts: part 1 consisted of deriving a dynamic sensing range (gauged via changes in the position of minimum reflectance R at resonance) and in identifying the region of highest sensitivity (gauged via changes in the slope of λ_{SPR}), all accomplished by simulations without experimental input. In both cases, Fabry–Perot (1)–(3) were applied with d_{Au} and θ_{SPR} independent variables as input parameters. An optimised sensor, then, would be the result of a compromise between optimal dynamic sensing range and the region of highest sensitivity. Part 2 utilised a blend of theoretical and experimental methodologies for the purpose of device characterisation.

The proposed characterisation scheme depended on the measurement of λ_{SPR} for different superstrate indices determined experimentally and subsequently fitted into calculations to estimate d_{Au} and θ_{SPR} . Incident angle dependence on d_{Au} at four different substrates with water superstrates were also calculated to determine specific λ_{SPR} . Experimental measurements of four chips with four combinations of superstrates were correlated with simulations. Part 3 involved enhancement of the SPR detector by application of PMMA thin films. Once again, concerted experimental and theoretical approaches were applied. The first derivative of results obtained in Part 2, as $d\lambda/dn$, were calculated to project sensitivity at varying d_{Au} at fixed θ_{SPR} based on the premise that sensitivity correlated with increasing slope.

2.1. Optimisation of the dynamic sensing and sensitivity ranges by simulations: Fabry–Perot equations, given in (1)–(3) below, were applied in simulations as no experimental component in Part 1. The overview of layered reflection schemes is shown in Fig. 2. A

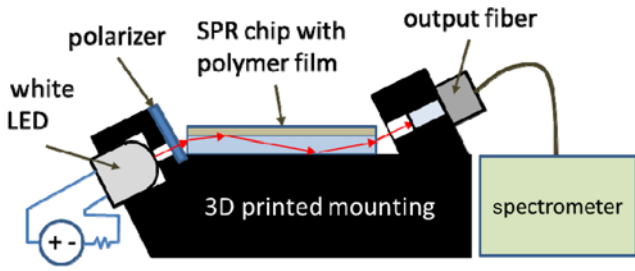


Fig. 1 BU-SPR system is depicted. An 'off-the-shelf' LED is shown in the light-side-coupling configuration. The housing was made by a simple 3D-printing technology with a printing resolution of $\pm 400 \mu\text{m}$

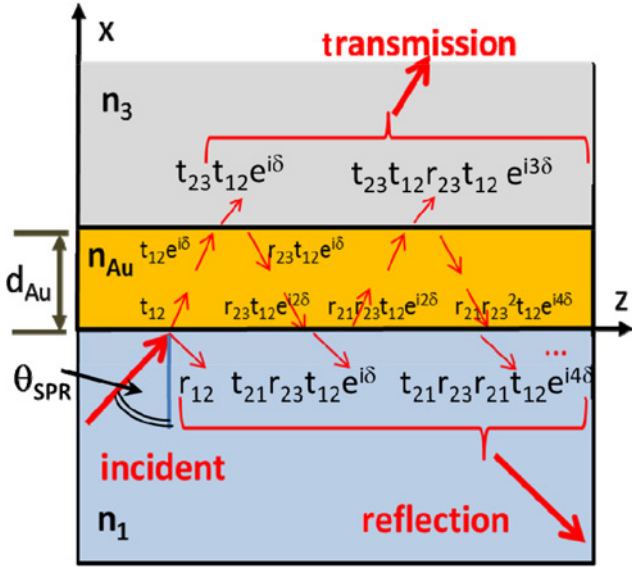


Fig. 2 Fabry-Perot model used in calculating the SPR response in three layers and interactions of a three-layered system (n_1 = glass, n_2 = Au and n_3 = water)

superstrate layer consisting of deionised (DI) water ($n_3 = 1.3324$) was applied to the gold surfaces in simulations as solution-based superstrate material is considered in the experimental part of the work. The refractive indices of the different materials used in all the calculations are obtained from the online refractive index database (www.refractiveindex.info)

$$r = r_{12} + \frac{t_{12}t_{23}r_{23}\exp(i2k_{x,Au}d)}{1 - r_{23}r_{21}\exp(i2k_{x,Au}d)} \quad (1)$$

where [12]

$$r_{2m} = -r_{m2} = \frac{\psi_2 k_{z,Au} - \psi_m k_{z,m}}{\psi_2 k_{z,Au} + \psi_m k_{z,m}}, \quad m = 1 \text{ or } 3 \quad (2)$$

and

$$k_{z,j} = k_o \sqrt{n_j^2 - (n_1 \sin \theta_{\text{SPR}})^2}, \quad (3)$$

$$\theta_{\text{SPR}} = \cos^{-1}(\sin \theta_o / n_1)$$

In (1)–(3), variables r and t are the reflectance and transmittance coefficients, respectively where $t_{mj} = 1 + r_{mj}$ where m and j have integer values 1, 2 or 3; k_z is the refractive index of the longitudinal (z) propagation constant and k_x is the transverse propagation

constant. The variable $\psi_j = 1$ for TE polarisation and $1/\epsilon_j$ for TM polarisation, where ϵ_j is the dielectric function for each layer. The specific refractive indices of each layer are n_1 (glass), and n_2 (n_{Au}) and n_3 (superstrate layer initially water). Fig. 3 shows the results of simulations as functions of d_{Au} and θ_{SPR} by application of these equations. To estimate the SPR wavelength for each condition (gold thickness and incident angle), a Python code was written using (1)–(3) to calculate the reflection spectrum. The SPR wavelength is extracted from the spectrum using the minimum finding algorithm.

In Fig. 3a, λ_{SPR} is plotted against gold layer thickness d_{Au} . Gold layer thickness was varied in simulations from 30 nm to a maximum of 70 nm. Each line in the graph represents a specific thickness-dependent SPR incident angle. Six θ_{SPR} values were input into the calculations: 69.0° , 69.6° , 70.1° , 71.0° , 73.0° and 77.2° representing the six curves depicted in the graph (refer to Fig. 1 for orientation). These values are selected to sustain practical SPR signal strength within the visible range for the reflected spectrum. The highest sensitivity was identified as the region of greatest change in the slope as given by $\Delta\lambda_{\text{SPR}}/\Delta d_{\text{Au}}$. According to simulations, this region of sensitivity was shown to be highest for thinner d_{Au} , nearest to the 30 nm boundary. Furthermore, sensitivity was more pronounced at lower values of θ_{SPR} (69.0° – 71.0°). Maximum sensitivity, therefore, is predicted to occur with thinner films of gold in concert with smaller SPR incident angles. On the other hand, the dynamic range of detection was predicted by simulations to occur for somewhat thicker gold layers, as shown in Fig. 3b. The dynamic range can be assumed to be different between reflectance off-resonance (≈ 1) and at resonance (R) or $1-R$. The value of $1-R$ at resonance is most pronounced in the range of 45–55 nm gold thickness. Finally, such first-order approximations of gold layer thickness and SPR incident angle constituted the first steps in enhancing device performance. By adopting such a calculation-based signal processing approach for experimental measurements, extensive characterisation by scanning electron

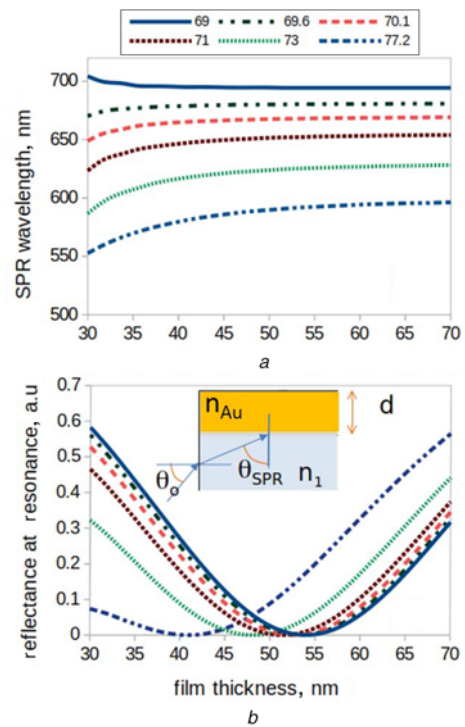


Fig. 3 Change of
a SPR wavelength
b Reflectance at resonance versus gold film thickness (from 30 to 70 nm) and SPR angle from (69.0° to 77.2°). Calculations were done with water superstrate

microscopy and other costly and time-consuming methods can be avoided. This is achievable through fitting the SPR angle and thickness parameters in the model to obtain a response similar to the experiment as will be illustrated in the experimental part.

3. Device characterisation scheme and optimisation: Fabrication of the BU-SPR device was described in a previous publication [10]. Briefly, the housing and support structures were made of polylactic acid (PLA) fabricated via a 3D printing method with 400 μm resolution. The fabrication of the SPR chip was accomplished using DC sputtering. The process involved cleaning of glass substrates and coating with a thin layer of chromium (~ 5 nm) followed by deposition of a gold layer to a targeted thickness of ~ 50 nm. Chromium is used to provide adhesion of gold to the 2 mm thick glass slide substrate. The coated glass slide is then cut into three equal pieces wherein each served as an SPR chip. The chip was tested by dropping 50 μL of the solution near the light excitation side to maximise the interaction. The targeted SPR angle was controlled through the 3D printed LED mounting. The configuration of the layers and superstrate were identical to the configuration displayed in Fig. 2. Theoretical and experimental methodologies were both applied in this part. The initial $\lambda_{\text{SPR-initial}}$ response was measured for three different experimental substrates with water as the superstrate layer in all cases. The experimental component was conducted within BU-SPR devices (Fig. 1). Initial $\lambda_{\text{SPR-initial}}$ measurements were performed first as a starting point to calculate d_{Au} and θ_{SPR} by simulation. Increasing the refractive index caused a red-shift in λ_{SPR} . Hence, an optimum combination of d_{Au} and θ_{SPR} produced the closest fit to both $\lambda_{\text{SPR-initial}}$ as well as the slope of the measurements. The calculations, using (1), were performed to find matching combinations of θ_{SPR} and d_{Au} that gave the same average λ_{SPR} . The changes of λ_{SPR} with refractive index were then recorded for each combination. From this exercise, combinations of d_{Au} and θ_{SPR} were extracted from normalised refractive index inputs. This approach is presented in Fig. 4 for three specific λ_{SPR} corresponding to three different water superstrates. The calculations were performed for three cases: $\lambda_{\text{SPR-initial}} = 576.8, 609.6$ and 656.8 nm correlating with the three experimental substrates. The Au film thickness was varied in the range between 30 and 50 nm.

As the plots indicate, the sensitivity was improved by increasing the effective index of the superstrate region. The effective index

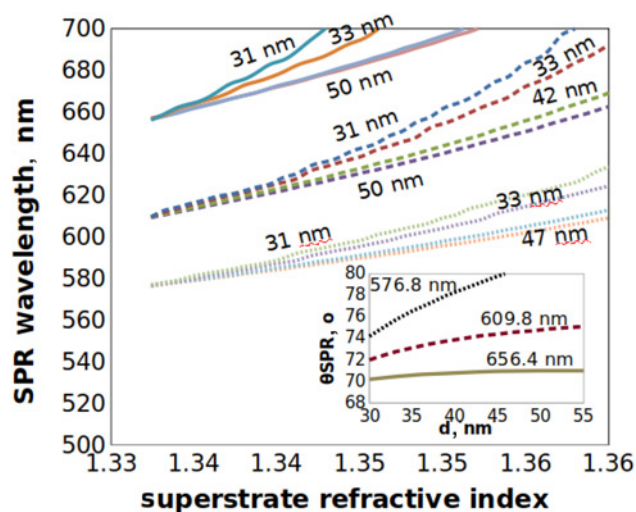


Fig. 4 Change of the SPR wavelength λ_{SPR} with superstrate refractive index for the combination of different gold thickness d_{Au} and incident angle θ_{SPR} . The inset shows simulations of three-chip substrates relating the incident angle as a function of gold layer thickness to produce λ_{SPR} for selective refractive indices. Water was the superstrate material in all cases

of the superstrate can be increased by adding a thin film of high refractive index polymer on top of the gold layer. In this study, PMMA was selected as high-index polymer. This is because of its low cost, low optical losses in the visible spectrum, long-term stability and reusability [13, 14]. In addition, a thin layer (in nm range) of PMMA was reported to be sensitive to different VOCs (such as Toluene) [15, 16] and volatile halo hydrocarbons like chloroform, dichloromethane (DCM) and trichloroethylene (TCE) with a very short response and recovery time [17, 18].

Device characterisation continued with actual data acquisition on substrates with superstrate combinations of materials of different refractive indices: water, toluene and chloroform. In Fig. 5a, λ_{SPR} is plotted as a function of increasing refractive index. Experimental results are represented by symbols and simulated data are represented by curves. The superstrates consisted of water mixed with either chloroform (refractive index at $20^\circ\text{C} = 1.4459$, solubility in water = 8.09 g/L at 20°C , density = 1.49 g/cm 3) or toluene (refractive index at $20^\circ\text{C} = 1.497$, solubility in water = 0.52 g/L at 20°C , density = 0.87 g/cm 3). It is not clear if there was adequate mixing in all cases, especially at higher concentrations, i.e. phase separations, to produce a homogeneous refractive index with great confidence. Nonetheless, experimental data trended well with simulated results. Experimentally, the precise thickness d_{Au} of the SPR chips was not known prior to characterisation. Also, the chips used were coated in two different patches. Hence the deposition conditions were different in both processes. Fabricated chips were placed manually on BU-SPR system and therefore may have contributed to inherent errors. The 3D printed mounting was designed to achieve θ_{SPR} of 73.0° . The error in printing and chip placement as well perhaps caused deviation from the desired angle. An error of 1° in the SPR angle for instance can cause a shift of 20 nm in the SPR resonance as indicated in Fig. 3a.

Calculations were generated to make best fits with experimental data. For Chip 1 (DI water and four different concentration of toluene in DI water: toluene/DI v/v% of 0, 0.02, 0.04, 0.06 and 0.08% were used). The $d_{\text{Au}} = 33$ nm provided the best fit in simulations; for Chip 2, $d_{\text{Au}} = 33$ nm; for Chip 3, $d_{\text{Au}} = 31$ nm; and finally for Chip 4, $d_{\text{Au}} = 30$ nm. In all cases except for Chip 2, the minimum thickness promoted in part 1 was adhered quite well. Chip 2, as it turned out, was made under a different sputtering regime and may be the cause of the deviation at $d_{\text{Au}} = 50$ nm.

In Fig. 4, simulations showed that device sensitivity increased with lower gold film thickness, higher λ_{SPR} and higher superstrate

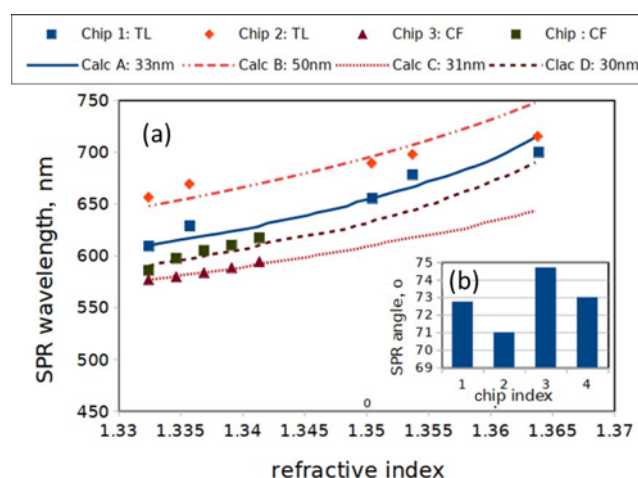


Fig. 5 Measured (symbols) and calculated (lines) SPR wavelength as a function of refractive index. The inset shows the estimated θ_{SPR} for the four chips

a Measured (symbols) and calculated (lines) SPR wavelength as a function of refractive index
b Estimated θ_{SPR} for the four chips

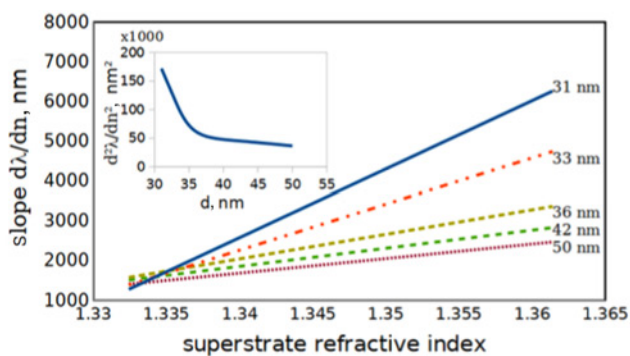


Fig. 6 Calculated sensitivity ($d\lambda_{\text{SPR}}/dn$) versus superstrate refractive index with varying gold layer thickness, all set at $\theta_{\text{SPR}} = 72.0^\circ$ and the second derivative (inset) versus gold film thickness

refractive index n_s . These are more fully visualised in Fig. 6 wherein the slope $d\lambda_{\text{SPR}}/dn$ is plotted against the superstrate refractive index for different gold layer thicknesses. θ_{SPR} was set constant at 72.0° which translated into $\lambda_{\text{SPR}} = 609.8$ nm for a water superstrate. In the graph, the slopes were calculated by fitting the curves in Fig. 4 to second-order polynomials. The inset in Fig. 6 shows the second derivative calculation versus gold film thickness. Most importantly, with all other aspects held constant, it can be seen that sensitivity was improved with increasing refractive index of the superstrate region.

In summary, this section presented a numerical method that allowed for the estimation of the gold film thickness of unknown SPR chip as well as the SPR angle for the system. The method used SPR measurements for different solutions with increasing refractive index. Fitting the measurement to the calculation, the authors were able to obtain good estimates of both d_{Au} and θ_{SPR} . In the next section, the results from Fig. 6 are utilised to further enhance the device sensitivity through increasing the effective index of the superstrate. This is done via coating of polymer thin film.

4. Sensitivity enhancement with PMMA layer: Enhanced sensitivity can be improved by increasing the effective refractive index of the superstrate region. The effective refractive index is defined by the combination of polymer refractive index and the solution within the extent of the evanescent wave on the surface (d_t in Fig. 7). This can be achieved uniformly by the application of a thin layer of PMMA onto the surface of the gold layer. PMMA was selected due to its relatively low cost, low optical losses, long-term stability and ease of application. PMMA has also been reported to be sensitive to organic compounds like toluene, chloroform, DCM and TCE. The SPR response to toluene and chloroform were studied in this work. The scheme is depicted in Fig. 7.

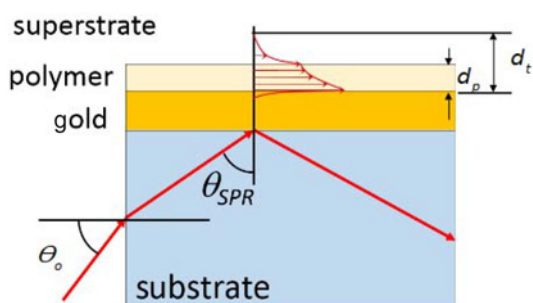


Fig. 7 PMMA layer is added to the system to enhance sensitivity. d_p is the polymer layer thickness and d_t is the dimension of the evanescent wave that penetrates to the gold layer. θ_0 is the incident light from the chip edge

The effective index, as in the case of a first-order approximation, can be expressed in (4) and (5) as

$$n_{\text{eff}} = n_s \times (1 - \eta) + n_p \times \eta \quad (4)$$

where d_t is the extension of the evanescent wave, d_p is the thickness of the polymer layer and the ratio $\eta = d_p/d_t$. n_s is the refractive index of the superstrate solution and n_p is the refractive index of the polymer layer.

The resultant effective index remained higher than that of the test solution so long as $n_p > n_s$. Increasing the effective index increased the detection slope as indicated in Fig. 6. Hence, the sensitivity was enhanced. One potential drawback in this scenario was that by addition of a polymer layer, the dynamic range of refractive index was decreased. Hence, the following expression of Δn_{eff} is given in (5)

$$\Delta n_{\text{eff}} = \Delta n_s \left(\frac{d_t - d_p}{d_t} \right) + \Delta d_p \left(\frac{n_p - n_s}{d_t} \right) + \Delta n_p \left(\frac{d_p}{d_t} \right) \quad (5)$$

For fixed polymer refractive index and thickness, the effective dynamic range is reduced by a factor of $1 - \eta$. Therefore, in order to increase sensitivity overall, the balance needs to be tilted in favour of higher slope in the effective refractive index over that of the reduced dynamic range.

Three identical chips were first prepared under identical conditions corresponding to ca. 30 nm gold layer thickness. PMMA-coated samples were compared to SPR chips without the coatings. Experimentally, two sets of PMMA coatings were prepared by spin-coating solutions consisting of PMMA dissolved in 1:1 v/v toluene/dichloroethane (DCE) solutions (of analytical grade and bought from Sigma-Aldrich Co. Ltd, USA). PMMA (Sigma-Aldrich Co. Ltd, USA) powder form with molar mass = 100.12 g/mol, melting point = 160° , density = 1.18 g/cm^3 , bead size, with average diameter, 20–25 nm was applied in two concentrations: 0.5 mg/mL (PMMA1) and 1.0 mg/mL (PMMA2). 5 ml solution was managed per sample. The mixtures were stirred for 2 h until all of the PMMA particles were dissolved. The solutions were then filtered through a polytetrafluoroethylene (PTFE) filter (pore diameter = $0.2 \mu\text{m}$) to eliminate precipitates and dust particles. Spin coating was accomplished via the static dispense technique onto clean gold-coated glass slides at 1000 rpm for 45 s. Acceleration and deceleration times were set to 5 s, respectively. In order to ensure uniform and smooth coatings, samples were first dried at room temperature for 12 h and then in an oven for 2 h at 80°C . As-prepared samples were then tested against SPR chips prepared without PMMA coatings.

Superstrates consisted of increasing concentrations of chloroform in DI water: 0, 2, 4, 6 and 8% chloroform by volume. Toluene was not tested in this part. Since all of these levels of chloroform exceeded its solubility limit in water (8.09 g/L), it was assumed that complete miscibility was not possible and that the superstrate existed in a state of divided phase in which the chloroform, being denser ($\rho = 1.49 \text{ g/cm}^3$), settled at the interface at PMMA layer. The refractive index of pure chloroform is 1.4459. However, calculations assumed a mixed homogeneous perhaps emulsified state. The performance of the devices under the conditions of PMMA1 and PMMA2 are depicted in Fig. 8. The plots in the figure clearly show increased slope as a function of PMMA thickness. The experimental slopes as λ_{SPR} versus chloroform concentration were found to be 376, 554 and 732 nm for uncoated, PMMA1 and PMMA2-coated chips, respectively. There was an increase in slope from PMMA1 to PMMA2 by a factor of 32% when PMMA concentration was doubled.

The graphs in Fig. 9 are plotted against chloroform concentration. To compare the experimental results with theory, the effective indices of the superstrate (in (4)) needed to be calculated for

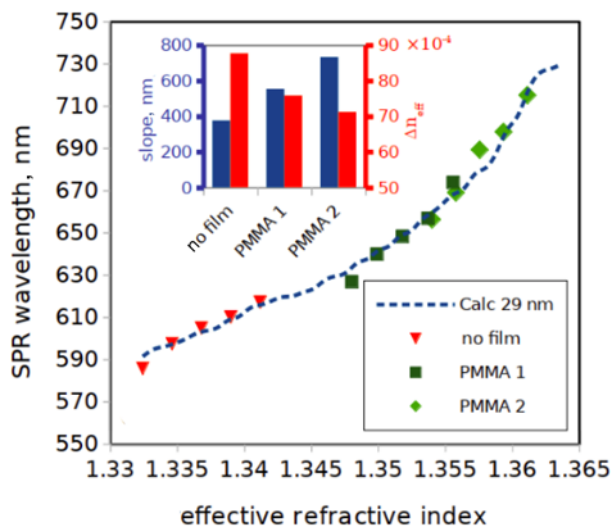


Fig. 8 Experimental data compared to calculations based on estimations of effective indices from (6)–(8). The inset shows slope enhancement, i.e. sensitivity, with a concomitant reduction in the dynamic range of the effective refractive index

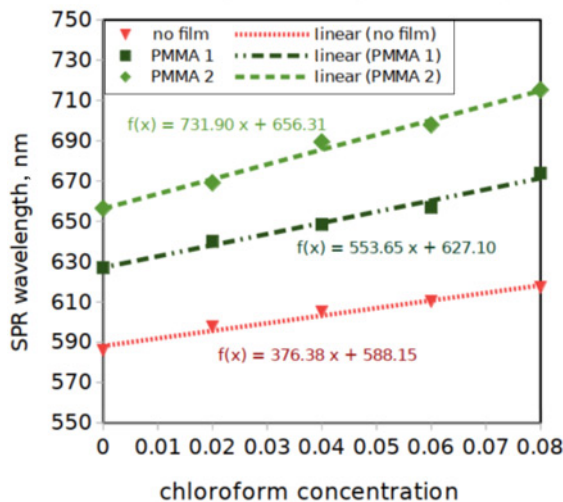


Fig. 9 Experimental SPR response of coated and non-coated chips for varying chloroform/water mixtures in terms of v/v

both polymer conditions and the different concentrations. That however, required knowing the ratio η , as well as, the polymers' refractive index. Polymer film refractive indices were estimated from the solution from known indices of toluene (1.4966) and DCE (estimated, 1.4125) as

$$n_p = n_{\text{PMMA}}\kappa + n_{\text{sol}}(1 - \kappa) \quad (6)$$

where n_p is the refractive index of the polymer film; κ is the concentration of PMMA in solution, n_{sol} is the refractive index of the composite solution wherein $n_{\text{sol}} = (n_{\text{Toluene}} + n_{\text{DCE}})/2$. The ratio η was not known as both thicknesses d_p and d_i were undetermined. It can be however estimated from the measured λ_{SPR} at 0 concentration (superstrate is pure DI water or $n_s = 1.3324$). Using the theoretical model for d_{Au} around 30 nm and θ_{SPR} around 72.0°, the effective index, n_{eff} , for polymer/water, was extracted from (4) by application of (7) wherein ratio η was calculated

$$\eta = 1 - \frac{n_{\text{eff},1} - n_{s,i}}{n_p - n_{s,i}} \quad (7)$$

Table 1 Estimated values for PMMA1 and PMMA2 used in constructing Fig. 8

Name	n_p	η	$n_{\text{eff},1}$ at $n_{s,1} = 1.3324$
PMMA1	1.4477	0.1354	1.3480
PMMA2	1.4479	0.1874	1.3542

where $n_{s,i}$ is the i th superstrate solution refractive index. Table 1 shows the estimated values in generating the λ_{SPR} versus effective refractive index curve shown in Fig. 8. These calculated effective indices were then applied to generate the curve.

Using the estimated value of the ratio η , the remaining effective refractive indices could be calculated via (4). Incidentally, it is worth noting that experimental results showed better fits in calculations when $d_{\text{Au}} = 29$ nm at $\theta_{\text{SPR}} = 72.5^\circ$ were considered as input parameters. The inset in Fig. 8 demonstrates improved slope, hence greater sensitivity, regardless of the reduced dynamic range of the effective refractive index. Also, from the definition of η on can roughly estimate the polymer film thicknesses for both PMMA1 and PMMA2 as 17 and 23 nm, respectively. Here, the evanescent beam extension, d_s , was estimated from the attenuation coefficient in the superstrate at the incident angle of 73° ($d_s \approx 120$ nm).

It is worth mentioning that for the PMMA film used in this analysis, a fluctuation in the temperature of five degrees around the room temperature causes a shift in the film index by 8×10^{-4} RIU [19, 20]. This fluctuation is within the detection limit of the BU-SPR [10]. According to (5) and Fig. 6, this can lead to SPR wavelength error in the range of 1.5 nm. However, in the experiment, the environment temperature was controlled to keep minimal temperature fluctuation.

5. Conclusion: This Letter presented an approach to enhance sensitivity by increasing the effective index of the sensing medium. This is done through coating a thin PMMA film with different concentrations. A model was proposed to indicate the SPR chip gold coating through successive measurements. The results show a clear increase in the measurement slope, by almost a factor of two, when increasing the effective index. The experimental results show a good agreement with the developed model.

6. Acknowledgments: The authors thank the Photonics Technology Laboratory and Smart Systems Lab at NECTEC, NSTDA, Thailand for their help in providing samples and help in the characterisation. The authors would like to also thank AIT for partially supporting the research work through their fellowship program.

7 References

- [1] Brantley H.L., Thoma E.D., Eisele A.P.: 'Assessment of volatile organic compound and hazardous air pollutant emissions from oil and natural gas well pads using mobile remote and on-site direct measurements', *J. Air Waste Manag. Assoc.*, 2015, **65**, (9), pp. 1072–1082
- [2] Chen X., Zhang T., Liang P., *ET AL.*: 'Original paper application of continuous-flow liquid phase microextraction to the analysis of phenolic compounds in wastewater samples', *Microchim. Acta*, 2006, **155**, (3–4), pp. 415–420
- [3] Hernandez-Vargas G., Sosa-Hernandez J.E., Saldarriaga-Hernandez S., *ET AL.*: 'Electrochemical biosensors: a solution to pollution detection with reference to environmental contaminants', *Biosens.*, 2018, **8**, (2), p. 29
- [4] The Cost-Effective Solution for Real-Time VOC and HAP Emission Measurements, Internet site, RJ Lee Group, rjg.com/wwp-content/uploads/2014/09/PTR-MS-for-OG.pdf, 2014

- [5] Ahmadian M., Jafari K.: 'A graphene-based wide-band MEMS accelerometer sensor dependent on wavelength modulation', *IEEE Sens. J.*, 2019, **19**, (15), pp. 6226–6232
- [6] Tai Y.H., Fu P.H., Lee K.L., *ET AL.*: 'Spectral imaging analysis for ultrasensitive biomolecular detection using gold-capped nanowire arrays', *Sensors (Basel)*, 2018, **18**, (7), pp. 1–10, doi. 3390/s18072181
- [7] Casalini R., Wilde J.N., Nagel J., *ET AL.*: 'Organic vapour sensing using thin films of a co-ordination polymer: comparison of electrical and optical techniques', *Sens. Actuat. B-Chem.*, 1999, **57**, (1–3), pp. 28–34
- [8] Feresenbet E.B., Dalcanale E., Dulcey C., *ET AL.*: 'Optical sensing of the selective interaction of aromatic vapors with cavitands', *Sens. Actuat. B-Chem.*, 2004, **97**, (2–3), pp. 211–220
- [9] Vlček J., Pištora J., Lesňák M.: 'Design of plasmonic-waveguiding structures for sensor applications', *Nanomaterials*, 2019, **9**, p. 1227
- [10] Somarapalli M., Koul K., Lahon R., *ET AL.*: 'Demonstration of low-cost and compact SPR optical transducer through edge light coupling', *Micro Nano Lett.*, 2017, **12**, (9), pp. 643–646
- [11] Gupta G., Kondoh J.: 'Tuning and sensitivity enhancement of surface plasmon resonance sensor', *Sens. Actuat. B-Chem.*, 2007, **122**, (2), pp. 381–388
- [12] Singh M., Holzinger M., Tabrizian M., *ET AL.*: 'Noncovalently functionalized monolayer graphene for sensitivity enhancement of surface plasmon resonance immunosensors', *J. Am. Chem. Soc.*, 2015, **137**, (8), pp. 2800–2803
- [13] Teich M.C., Saleh B.E.A.: 'Fundamentals of photonics' (John Wiley & Son, New York, USA, 1991, 3rd edn.)
- [14] Adhikari B., Majumdar S.: 'Polymers in sensor applications', *Prog. Polym. Sci.*, 2004, **29**, (7), pp. 699–766
- [15] Sasaki D.Y., Singh S., Cox J.D., *ET AL.*: 'Fluorescence detection of nitrogen dioxide with perylene/PMMA thin films', *Sens. Actuat. B Chem.*, 2001, **72**, (1), pp. 51–55
- [16] Matsuguchi M., Uno T.: 'Molecular imprinting strategy for solvent molecules and its application for QCM-based VOC vapor sensing', *Sens. Actuat. B-Chem.*, 2006, **113**, (1), pp. 94–99
- [17] Vassiltsova O.V., Zhao Z., Petrukhina M.A., *ET AL.*: 'Surface-functionalized CdSe quantum dots for the detection of hydrocarbons', *Sens. Actuat. B-Chem.*, 2007, **123**, (1), pp. 522–529
- [18] Li Y., Wang H.-C., Yang M.-J.: 'n-Type gas sensing characteristics of chemically modified multi-walled carbon nanotubes and PMMA composite', *Sens. Actuat. B-Chem.*, 2007, **121**, (2), pp. 496–500
- [19] Kedenburg S., Vieweg M., Gissibl T., *ET AL.*: 'Linear refractive index and absorption measurements of nonlinear optical liquids in the visible and near-infrared spectral region', *Opt. Mater. Express*, 2012, **2**, (11), pp. 1588–1611
- [20] Kasarova S.N., Sultanova N.G., Nikolov I.D.: 'Temperature dependence of refractive characteristics of optical plastics', *J. Phys.: Conf. Ser.*, 2010, **253**, p. 012028